Near Edge X-Ray Absorption Fine Structure Spectroscopy Studies of Single-Crystalline V_2O_5 Nanowire Arrays

By *Jesus M. Velazquez,*[1] *Cherno Jaye,*[2] *Daniel A. Fischer,*[2] and *Sarbajit Banerjee*[1*]

[1.] Department of Chemistry, University at Buffalo, State University of New York, Buffalo, NY 14260-3000

[2.] Materials Science and Engineering Laboratory, National Institute of Standards and Technology, Gaithersburg, MD 20899

E-mail: sb244@buffalo.edu

Abstract

Near edge X-ray absorption fine structure (NEXAFS) spectroscopy is used to precisely probe the alignment, uniformity in crystal growth direction, and electronic structure of single-crystalline V_2O_5 nanowire arrays prepared by a cobalt-catalyzed vapor transport process. The dipole selection rules operational for core-level electron spectroscopy enable angle-dependent NEXAFS spectroscopy to be used as a sensitive probe of the anisotropy of these systems and provides detailed insight into bond orientation and the symmetry of the frontier orbital states. The experimental spectra are matched to previous theoretical predictions and allow experimental verification of features such as the origin of the split-off conduction band responsible for the *n*-type conductivity of V_2O_5 and the strongly anisotropic nature of vanadyl-oxygen-derived (V=O) states thought to be involved in catalysis. The strong anisotropy observed across thousands of nanowires in the NEXAFS measurements clearly demonstrates the uniformity of crystal growth direction in these nanowire arrays.

Introduction

The fabrication of 1D nanostructures such as nanotubes and nanowires exhibiting remarkable finite size effects as a result of their anisotropy and quantum confinement has spurred tremendous growth and interest in the emerging areas of nanoelectronics and nanophotonics.[1-3] These nanostructures have been heralded as potential building blocks for integration within multifunctional electronic and optoelectronic devices incorporating significant complexity and enabling massive miniaturization with large increases in device density.[4,5] Much progress has been achieved in recent years in fabricating single-crystalline arrays of II—VI and III—V semiconductor nanowires, carbon nanotubes, and nanostructures of some binary metal oxides such as ZnO by chemical vapor deposition and templated electrochemical techniques.[3,6-8] However, relatively little progress has been achieved in preparing nanostructured cathode materials based on vertically aligned arrays of nanowires despite the clear benefits that can be expected from the fabrication of novel battery architectures and their use as power sources in applications ranging from implantable defibrillators to hybrid vehicles. In a recent report, we demonstrated the fabrication of large-area vertically aligned arrays of single-crystalline 1D V_2O_5 nanowires on Si/SiO_2 substrates by the catalyzed vapor transport of V_2O_4 and V_2O_5 precursors establishing considerable control over the nanowire dimensions and substrate coverage.[9] Here, we demonstrate the use of angle-dependent near edge X-ray absorption fine structure (NEXAFS) spectroscopy to study the electronic structure and alignment of these highly anisotropic nanowires. The results are compared to fairly detailed electronic structure calculations that have been reported in the literature and provide experimental verification for predictions of the specific V 3*d* and O 2*p* orbitals that give rise to the highly anisotropic optical absorbance, electrical conductivity, and Li-ion intercalation properties of these systems.[10,11] NEXAFS

spectroscopy using linearly polarized synchrotron radiation is further shown to be a useful probe of the degree of alignment, uniformity of crystal growth direction, and crystalline order of these systems.

V_2O_5 crystallizes in an orthorhombic structure (*Pmmn*) based on zigzag double layers of distorted VO_5 square pyramids sharing edges and corners with the layers separated by a pronounced van der Waals' gap, as illustrated in **Figure 1**.[12,13] Figure 1B depicts the unit cell of orthorhombic V_2O_5 containing 14 atoms corresponding to two formula units. The layers themselves are weakly bound by electrostatic forces along the *c*-axis and the spacing between the layers provides abundant sites for the facile intercalation of various inorganic and organic guest species.[14,15] Three distinct and crystallographically inequivalent oxygen atoms can be identified in the crystal structure of V_2O_5, as shown in Figure 1A. Singly coordinated terminal/apical vanadyl oxygens have a relatively short V—O bond length of about 1.577 Å (O1);[16] in addition, the zigzag layers also contain bridging oxygen atoms linking two vanadium-centered polyhedra via corner-sharing interactions (O2) and chaining oxygen atoms linking three [VO_5] polyhedra via edge-sharing interactions (O3).[17,18] An alternative description of the orthorhombic V_2O_5 structure is to consider highly distorted [VO_6] octahedral building blocks linked together to form the layered anisotropic structure; the vanadium and vanadyl oxygen atoms are shifted from the octahedral centers to give rise to a short V—O bond as mentioned above and also a much longer V—O bond to an apical oxygen in the next layer with a bond length estimated to be about 2.791 Å.[16] Such a [VO_6] octahedron would thus contain two apical vandyl oxygens (with one short and one very long V—O bond), one bridging oxygen involved in corner sharing, and three triply-coordinated chaining oxygen atoms involved in edge sharing, thus yielding an intrinsically anisotropic layered structure.

The layered structure of V_2O_5 and the readily accessible V^{5+}/V^{4+} redox couple makes it an especially attractive system for use as a cathode material in Li-ion batteries based on the reversible insertion and extraction of Li-ions from interlayer sites.[12,13,19] Most notably, the intercalation voltage in V_2O_5 is very well matched with the stability window of polymer electrolytes that have been developed for Li-ion—polymer batteries to power electric and hybrid vehicles.[20] However, bulk V_2O_5 is beset by several problems such as sluggish Li-ion intercalation/deintercalation kinetics and irreversible lithiation for $Li_xV_2O_5$ stoichiometries at high x values.[13,21] Scaling V_2O_5 to nanoscale dimensions offers the potential for increased power and energy densities because of shorter cathode diffusion path lengths, an improved electrolyte interface, and the operation of Li-ion storage mechanisms not accessible in the bulk.[22-24] Recently, Cui and co-workers have demonstrated the completely reversible lithiation and delithiation of sub-100 nm diameter nanowires even for lithiated phases $Li_xV_2O_5$ with x approaching 3.0.[22] Indeed, these authors have articulated the need for a novel battery architecture based on arrays of highly oriented V_2O_5 nanowires grown on a collector electrode wherein the power rates are limited only by the charging/discharging of individual nanowires.[22] The single-crystalline nanowire arrays of V_2O_5 fabricated by our catalyst-assisted vapor transport process fulfill this need and may also be useful for other applications that exploit the intrinsic anisotropy of the V_2O_5 crystal structure such as thermally/electrically activated optical switching devices, write-erase media, optical waveguides, and microreactor catalyst beds.[25,26] For most of these applications, it is desirable that the nanowires conform to a uniform growth direction and show a high degree of alignment. Here, NEXAFS spectroscopy is also demonstrated to be a sensitive probe of the extent of alignment of the nanowire arrays.

NEXAFS spectroscopy involves the use of soft X-rays to promote electrons from core levels to partially filled and empty states and is thus a powerful local element-specific probe of the electronic structure above the Fermi level.[27,28] The dipole selection rules for NEXAFS require that there be no change in the spin of the excited electron and that the change in the angular momentum quantum number, $\Delta l = \pm 1$. This implies that for the excitation of an O 1*s* electron, only states with some O 2*p* character can be reached. The peak positions and lineshapes of the obtained resonances are thus closely correlated to the unoccupied density of states projected onto the excited atom (as modified by self-energy effects).[27] In recent years, NEXAFS spectroscopy has emerged as a sensitive probe of the electronic structure of transition metal oxides owing to the strong hybdrization of O 2*p* states with transition metal *d* orbitals, which gives rise to finely structured features containing a wealth of information about bonding and electronic structure for early transition metal oxides.[28,29] The NEXAFS dipole selection rules also give rise to the "searchlight effect" wherein different frontier orbital states can be observed depending on their symmetry and spatial orientation by varying the angle of incidence of the linearly polarized X-ray beam, thus making NEXAFS spectroscopy an excellent probe of the anisotropy and bond orientation of different materials.[27] For example, in recent work NEXAFS spectroscopy has been used to evidence the order and alignment of carbon nanotube arrays and films with considerable surface sensitivity.[30,31] Here, we use angle-dependent NEXAFS spectroscopy to probe the electronic structure and alignment of V_2O_5 nanowire arrays.

Experimental

***Synthesis of V_2O_5 Nanowire Arrays*:** The single-crystalline V_2O_5 nanowire arrays were fabricated on Si/SiO_2 substrates using a recently developed protocol based on the catalytic vapor phase oxidation of V_2O_4 to V_2O_5 in an Ar/O_2 atmosphere according to

$2VO_2 + 0.5O_2 \rightarrow V_2O_5$ (1).[9]

Briefly, a Co catalyst layer with thickness ranging from 1.5-10.0 nm was evaporated onto a clean Si/SiO_2 substrate using an electron-beam evaporator at a pressure $<1\times10^{-5}$ torr. The Co-coated substrate was then placed in a 1" quartz tube within a homemade CVD reactor based on a single-zone tube furnace at temperatures ranging from 300—450°C and pressures $<10^{-3}$ torr. A ceramic boat containing micrometer-sized VO_2 powder (Aldrich, >99%) was placed at the center of the tube furnace and heated to 900°C under a flow of 47/3 sccm of Ar/O_2 using a flow mixer to precisely control the mixing of the gases. The best results in terms of orientation and surface coverage were obtained after reaction for 1—2 h; some crystal overgrowth was noted after longer time periods.

***Characterization*:** Scanning electron microscopy (SEM) images were acquired on a Hitachi SU-70 instrument equipped with an EDX detector at an accelerating voltage of 20 kV. A JEOL JEM 2010 instrument operated at 200 kV was used to acquire high-resolution transmission electron microscopy (HRTEM) images of the nanowires. To prepare the samples for TEM observations, chips with the V_2O_5 nanowire arrays were ultrasonicated in 2-propanol solution and a razor blade was used to harvest the nanowires from the substrate. A drop of the solution was placed on a 300 mesh carbon-coated Cu grid for TEM measurements. X-ray diffraction (XRD) patterns were acquired using a Siemens D-500 instrument using Cu Kα radiation.

***NEXAFS Spectroscopy*:** Near edge X-ray absorption fine structure (NEXAFS) spectroscopy data was collected on National Institute of Standards and Technology beamline U7A at the National Synchrotron Light Source of Brookhaven National Laboratory with a toroidal mirror spherical grating monochromator using a 1200 lines/mm grating with a nominal energy resolution of 0.1 eV. NEXAFS spectra were collected in partial electron yield mode with a

channeltron multiplier near the sample surface using the detector at −200 V bias to enhance surface sensitivity. A charge compensation gun was used to prevent the charging of the samples. A freshly-evaporated vanadium mesh was used as a reference standard for every individual spectra ensuring careful calibration of the energy scale. To eliminate the effect of incident beam intensity fluctuations and monochromator absorption features, the partial electron yield signals were normalized using the incident beam intensity obtained from the photoemission yield of a clean Au grid with 90% transmittance measured upstream from the sample. The V L-edge and O K-edge spectra were acquired in a single scan for samples mounted using Cu tape onto a sample holder within the UHV chamber. Pre- and post-edge normalization of the data was performed using the Athena suite of programs.

Results and Discussion

The nanowires obtained by the catalytic vapor transport process using a 1.5 nm thick Co film as the catalyst are about 65±20 nm in diameter although nanowires with diameters <30 nm are also observed. **Figures 2A and B** show SEM images of dense vertically aligned nanowire arrays showing the smooth walls and uniform thickness along the length of the nanowires. The growth of the nanowires is thought to proceed via a vapor—solid process first involving the formation of howardevansite and lyonsite-type cobalt vanadate phases upon the alloying of the V_2O_5 nuclei formed in situ as per Eq. 1 with Co nanoparticles.[9,32] In the absence of the Co catalysts, nanowire arrays have not been observed. Nanowire growth appears to proceed via a root-growth mechanism wherein incoming V_2O_5 vapor is added at the nanowire/catalyst interface with the catalyst particle strongly decreasing the barrier for the incorporation of the V_2O_5 vapor and providing a much greater sticking coefficient than the bare substrate.[9,33] Consistent with such a root-growth mechanism, Co particles have not been found at the faceted

tips of the nanowires, as shown in Figures 2c and d. HRTEM images such as shown in Figure 2d corroborate the single-crystalline nature of the nanowires. **Figure 3** contrasts a representative XRD pattern acquired for a vertically aligned nanowire array grown for 1 h with the diffraction pattern for bulk V_2O_5 powder; only the characteristic (00*h*) peaks of orthorhombic V_2O_5 (Joint Committee on Powder Diffraction Standards (JCPDS #41-1426)) are visible, indicating the strongly preferential growth direction of these nanowires and the strong anisotropy of the nanowire arrays.

To quantitate the anisotropy within the nanowire arrays, evaluate the uniformity of the crystal growth direction, and obtain a detailed understanding of the electronic structure of these nanowires, V L-edge and O K-edge NEXAFS spectra have been obtained for the nanowire arrays, as shown in **Figure 4**. Given the NEXAFS selection rules noted above, the V L-edge NEXAFS spectra represent the *d*-projected unoccupied density of states, whereas the O K-edge spectra provides an image of the *p*-projected unoccupied density of states of the frontier levels.[29,34] The two broad peaks centered at ~518 and 525 eV are the V L_{III} and L_{II} peaks arising from V2$p_{3/2}$→V3*d* and V2$p_{1/2}$→V3*d* transitions, respectively. The spin-orbit splitting between the V L_{III} and L_{II} peaks is 6.9 eV for the V_2O_5 nanowires compared to the ~7.5 eV splitting observed in V 2*p* X-ray photoelectron spectroscopy (XPS) data for the same sample. The difference in the spin-orbit splitting can be attributed to self-energy effects; the interaction of the excited electron with its surroundings alters the density of states to different extents in XPS and NEXAFS because of the different final states of the excited electron in the two processes.[29] The V L_{II} peak is broadened by a Coster—Kronig Auger decay process into a 2$p_{3/2}$ hole and is less informative than the V L_{III} peak in interpreting the electronic structure of the V_2O_5 nanowires.[35,36] The V L_{III} peaks shows considerable fine structure that is significantly dependent

on the angle made by the sample to the polarization vector **E** of the incident beam. The strong polarization dependence of the peaks originates from the highly anisotropic crystal structure of V_2O_5 and the specific orientation of the V 3*d* orbitals that contribute to bands above the Fermi level due to crystal field splitting (vide infra).

The peaks labeled as O K-edge peaks in Figure 4 correspond to transitions from oxygen 1*s* to states with some O 2*p* character.[29] The O 2*p* orbitals in V_2O_5 are strongly hybridized with the narrow V 3*d* orbitals and thus the finely structured O K-edge spectra provides significant insight into the frontier orbital states involved in bonding in V_2O_5.[36] The considerable intensity of the O K-edge features relative to the V L-edge resonances indicates the significant covalent character of the V—O bonds in V_2O_5, as is typical of early transition metal oxides (the shrinking size of *d* orbitals somewhat reduces covalent contributions to bonding in later transition metal oxides).[29,37] The splitting of the O K-edge peaks can be attributed to the roughly octahedral crystal field splitting of the V 3*d* levels upon hybridization with the O 2*p* levels. Despite the strong distortion from octahedral symmetry, *ab initio* density functional theory (DFT) calculations indicate that the V 3*d* levels are split approximately by a cubic field into t_{2g} and e_g levels in the O-projected unoccupied density of states.[16,38] **Table 1** shows the V 3*d* orbitals that are hybridized with the different O 2*p* orbitals based on a molecular orbital picture assuming distorted octahedral crystal field splitting.[16] The low-energy peak in the O K-edge spectra has t_{2g}-like symmetry and arises from the π interactions between the O 2*p* levels and V $3d_{xy}$, $3d_{xz}$, and $3d_{yz}$ levels; the high-energy O K-edge component arises from σ interactions between O 2*p* orbitals and V $3d_{x2-y2}$ and $3d_{z2}$ orbitals that are directly pointed towards the oxide ligands (**Table 2** and vide infra). The relative energies of the two peaks are justified by considering that the latter interactions are stronger and thus yield lower lying filled levels in the valence band and

higher lying anti-bonding levels in the conduction band of V_2O_5.[16] The separation between the two peaks corresponds to the ligand field splitting corrected for covalent contributions. The O K-edge peaks also show very strong polarization dependence originating from the distinctive hybridization of the O $2p_x$, $2p_y$, and $2p_z$ levels with different V 3*d* orbitals.

The weakly structured spectral features observed 5—10 eV above the threshold beyond 536 eV correspond to transitions from O 1*s* core levels to O 2*p* levels hybridized with V 4*s* and 4*p* states. The considerable spectral weight in this region indicates the substantial contributions from 4*sp* hybridization and further corroborates the strong covalent contributions to bonding in V_2O_5.[29,37]

Several detailed DFT calculations have been published in the literature in recent years that carefully map out the V and O projected density of states in V_2O_5 both above and below the Fermi level.[16-18,36,38,39] Some recent studies such as by Kolczewski and Hermann even take into account core-hole relaxation effects, yielding fairly detailed angle-dependant NEXAFS spectra as a function of polar and azimuthal angles.[38,39] These studies present some interesting arguments and have not yet been entirely experimentally verified due to the difficult in growing high-quality single crystals of V_2O_5. Nonetheless, the calculated density of states plots are extremely useful for understanding the spectral features and polarization dependence of the V L-edge and O K-edge spectra obtained here.

Figure 5 shows the angle-dependent V L-edge spectra measured for the V_2O_5 nanowire arrays. Based on studies of V_2O_5 single crystals, at least six different peaks can be identified for spectra acquired at grazing and normal incidence,[36] as marked in Figure 4, although the separation between V4 and V5 peaks is less clear in the nanowire samples than in single crystal samples reported previously in the literature likely because of the relatively greater degree of

disorder and the presence of faceted tips in the nanowire arrays. The observed peaks correspond not to transitions into distinct levels but to maxima in the V 3*d* unoccupied density of states of V_2O_5. The angle-dependent intensities of the different peaks mirror the specific contributions from orbitals with different spatial orientations to these discrete maxima since the relative spectral weight of a peak is essentially correlated to the number of unoccupied states that have the correct symmetry and orientation for an allowed transition from the core level. For normal incidence ($\theta = 90°$), the polarization vector **E** is parallel to the V_2O_5 *ab* plane ($\perp$ to the *c* axis), whereas for grazing incidence ($\theta = 20°$), **E** has a significant component parallel to the *c* axis. In the latter case, dipole selection rules allow for transitions from V 2*p* to V $3d_{xz}$, $3d_{yz}$, and $3d_{z2}$ states, whereas for normal incidence (**E** $\parallel$ to the *ab* plane) transitions to all five *d* orbitals are allowed. Figure 4 indicates that the lowest energy peak (V1) closest to the Fermi level increases in intensity and becomes sharply structured as the angle of incidence is increased and the polarization vector becomes parallel to the *ab* plane. This observation is consistent with the predominantly V $3d_{xy}$ origin of this band predicted by Eyert and Hock.[16] These authors have suggested that a narrow (~0.45 eV in width) split-off conduction band is formed just above the Fermi level and is separated by about 0.35 eV from the higher energy conduction band that is a convolution of 18 different bands. The V $3d_{xy}$ orbital is weakly hybridized with $2p_x/2p_y$ orbitals on the trigonally coordinated chaining oxygen atoms that enable edge sharing (labeled O3 in Fig. 1, Table 1).[16] This weak π overlap is reflected in the relatively long bond lengths, high-lying position in the valence band, and the formation of the split-off conduction band closest to the Fermi level (smallest bonding—antibonding splitting).[10,16,40] The angle dependence of this band observed in Figs. 3 and 4 is thus consistent with the proposed weak π-bonding V $3d_{xy}$-O $2p_x/2p_y$

origin of this level (Table 1). This localized split-off state at the bottom of the conduction band is thought to be responsible for the small and highly anisotropic *n*-type conductivity of V_2O_5.

The higher energy region of the V L-edge shown in Figure 5 bears remarkable similarity to the V 3*d*-projected unoccupied density of states calculated by Eyert and Hock.[16] These authors have demonstrated that despite the lowering of symmetry because of strong distortion from ideal octahedral geometry, the predominant splitting of states in the conduction band occurs along the lines of octahedral crystal field splitting into t_{2g} and e_g levels. There is almost complete separation of these levels at the V L-edge with the t_{2g} states lying between ~1.75—4.5 eV above the Fermi level and the e_g states appearing at energies >4.5 eV. This sharp splitting is a result of the differential hybridization of the V 3*d* levels with the O 2*p* levels, as shown in Table 1. The V e_g orbitals form stronger σ bonds with the O *2p* states giving rise to much greater bonding—antibonding splitting; in contrast, the t_{2g} levels interact with O 2*p* states via weaker π interactions resulting in higher lying filled states in the valence band and lower-lying empty states in the conduction band (weaker bonding—antibonding splitting).[16] The peak labeled V2 in Figure 4 can be ascribed to transitions to V $3d_{xy}$ states hybridized with O $2p_x$ and $2p_y$ orbitals on the bridging oxygen atoms involved in corner sharing (labeled O2 in Fig.1), and has the greatest intensity for normal incidence. The peak labeled V3 at slightly higher energy is likely derived from transitions to V $3d_{xz}$ and $3d_{yz}$ states hybridized with O $2p_x$ and $2p_y$ orbitals on the vanadyl oxygen atoms (O1) and starts to emerge as the angle of incidence is decreased and **E** has a greater component along the *c* axis. The peaks at still higher energy, >4 eV above threshold, are primarily e_g in origin. The narrowing and shift of these features in Figure 5 to higher energies with decreasing angle of incidence is consistent with the $3d_{z2}$ origin of the higher energy component of this peak. The $3d_{z2}$ orbital is strongly hybridized with the O $2p_z$ orbital of the

vanadyl oxygen resulting in the strong observed angle-dependence of this component, which essentially disappears when **E** is parallel to the *ab* plane (normal incidence).

Figure 6A shows the angle-dependent O K-edge NEXAFS data acquired for the nanowire array sample. For normal incidence, dipole selection rules allow transitions from O 1*s* to all the O 2*p* orbitals, whereas for grazing incidence when **E** is almost parallel to the long axis of the nanowires only transitions into the O $2p_z$ orbital are allowed. For normal incidence, Figure 6A shows that the Ox_1 peak dominates the spectrum. However, as the angle of incidence is decreased and the polarization vector moves out of the plane, the intensity of the Ox_1 peak decreases and the Ox_2 and Ox_3 peaks grow substantially in intensity. Figure 6B shows the data acquired at grazing incidence fitted to three distinct Gaussian components. The observed angle dependence suggests that the bands nearest to the Fermi level have predominantly O $2p_x$ and $2p_y$ symmetry and that the high-energy peak arises from a transition to states with a significant O $2p_z$ component. These assignments show remarkably good agreement with periodic linear combination of atomic orbitals (LCAO) and more recent DFT calculations of the O-2*p* projected unoccupied density of states.[16,17,36,40] Table 2 shows the contributions from final state levels with different orbital characters predicted by Kolczewski and Hermann for the three crystallographically inequivalent oxygen atoms.[38,39] These authors have performed a detailed *ab initio* DFT calculation predicting the angular dependence of the 1*s* core excitation spectra for V_2O_5 using a $V_{10}O_{31}H_{12}$ cluster as a model system and taking into account electronic core hole relaxation effects.[17,38,39] Indeed, the data presented in Figure 6 closely matches their predictions even reproducing the double peak high-energy structure predicted for grazing incidence. These authors had commented on the lack of availability of high-quality experimental data to verify the predictions. The data presented here accurately verifies the predictions indicating that it is

possible to distinguish between the three crystallographically inequivalent oxygen atoms in these anisotropic layered structures by varying the polarization of the incident beam. For the vanadyl or apical oxygens (O1), the V—O bond is oriented in the *z* direction and thus primarily involves the strongly directional σ overlap of O $2p_z$ with V $3d_{z2}$ orbitals, giving rise to a strong bonding—antibonding splitting; the transition from O1*s* to the antibonding states for this interaction thus appears at higher energy. In contrast, the O $2p_x$ and p_y orbitals on the vanadyl oxygen are involved in weaker π interactions with V $3d_{yz}$ and $3d_{xz}$ orbitals and appear at lower energies in the O K-edge NEXAFS spectra (contributing to Ox_1). For the doubly coordinated bridging oxygen atoms (O2) involved in corner sharing, the $2p_x$ orbitals point along the bond direction and form strong σ overlaps with V$3d_{x2-y2}$ orbitals (Table 2). Consequently, transitions into the antibonding levels for this interaction appear at higher energy than for $2p_y$—V $3d_{xy}$ π overlap that is perpendicular to the bond direction (and contributes to the low energy peak Ox_1). The triply coordinated O3 atoms involved in edge sharing show very different bond orientations from the O1 and O2 atoms.[38] The O $2p_x$ and $2p_y$ orbitals are both involved in σ-bonding to V $3d_{x2-y2}$ orbitals although given the trigonal coordination of the oxygen atoms, the σ-overlap is slightly weaker and less directional than for the bridging and vanadyl oxygen atoms. The predicted superposed excitation spectra for the excitation of the three different O atoms taking account their relative stoichiometries suggests that the vanadyl oxygens (O1) make the greatest contribution to the lower energy peak Ox_1, whereas the chaining oxygen (O3) makes the greatest contribution to the higher-energy components, Ox_2 and Ox_3.[38] The experimental data (Fig, 6 and Table 2) is clearly consistent with the symmetry of these states. Notably, the ionization potential of the three atoms is remarkably similar and X-ray photoelectron spectroscopy is unable to distinguish between these three species since only a broad O 1*s* peak is obtained, underlining the

importance of NEXAFS spectroscopy in precisely probing the strength and directionality of bonding within the distinctive oxygen sites. Consistent with the in-plane π interactions contributing to the low-energy peak Ox_1, the integrated intensity of the low-energy peak can be fitted to the function

$$I(\theta) = a + b\cos 2(\theta - \gamma) \qquad (2)$$

where γ is defined as the tilt angle and the normalized amplitude (b/a) is related to the order parameter of the transition dipole moment.[30,31,41] Such an order parameter is typically used to describe the degree of order in polymeric or carbonaceous systems but may also be helpful in evaluating the degree of alignment in nanowire arrays such as the ones studied here. For a completely randomly oriented sample an order parameter of 0 is expected. For HOPG graphite with π* orbitals perpendicular to the plane of the sample an order parameter of 1 is expected and indeed experimental data suggests an order parameter of 0.921 for a freshly cleaved sample.[30] An order parameter of −0.425 is calculated based on Figure 6C for the V_2O_5 nanowire arrays, which indicates a relatively high degree of order and uniformity in the nanowire growth direction. In comparison, for "polycrystalline" polymer systems, values >0.1 are thought to be indicative of substantial ordering.[41] Indeed, measurements of carbon nanotube arrays have typically yielded order parameters <0.15.[31] A further orientation parameter, the dichroic ratio (*DR*) is also commonly used to evaluate order and has been determined here by extrapolating the integrated intensity of the O K-edge t_{2g} peak to $\theta = 0°$. The dichroic ratio is defined as:

$$DR = \frac{(I_\perp - I_\parallel)}{(I_\perp + I_\parallel)} \qquad (3)^{42}$$

where $I_\perp$ is the integrated intensity of the t_{2g} peak at $\theta = 90°$ and $I_\parallel$ is the extrapolated intensity at $\theta = 0°$ as described above.

For the nanowire samples, a value of 0.45 has been derived using the data shown in Figure 6. As comparison, a freshly cleaved atomically perfect HOPG graphite sample has been shown to have a DR value of -0.90 with the negative sign indicating that the integrated intensity decreases with increasing angle of incidence (π orbitals are perpendicular to that in our V_2O_5 nanowire arrays). Carbon nanotube arrays have been shown to have DR values ranging from 0.03—0.14 and carbon nanotube films have DR values of ~-0.1.[30,31] Both evaluations of the degree of alignment thus indicate a high degree of order and uniformity of crystal growth direction in the V_2O_5 nanowire arrays. The faceted nature of the nanowire tips and the presence of some disorder due to the leaning of longer nanowires likely contribute to the decrease in order from the theoretically predicted value of 1.

In conclusion, NEXAFS spectroscopy has been used to evidence the high alignment and uniform crystal growth direction of single-crystalline V_2O_5 nanowire arrays prepared by a novel catalyzed vapor transport process. The nanowire arrays also serve as excellent model systems to verify detailed calculations of the electronic structure of V_2O_5. Angle-dependant NEXAFS measurements of these anisotropic structures allow specific bond orientations to be probed. Most notably, the V L-edge spectra are consistent with the formation of a low-energy split-off conduction band below the higher energy part of the conduction band arising from the weak π interactions between V $3d_{xy}$ and O $2p_x$ and $2p_y$ orbitals on the chaining oxygen atoms involved in edge-sharing. The O K-edge spectra corroborate the strong contribution of the highly oriented V—O bond of the vanadium center with the terminal vanadyl oxygen (predicted to arise from V $3d_{z2}$—O $2p_z$ interactions) to the high energy O K-edge peak and suggest that angle-dependant NEXAFS spectroscopy may indeed be useful to selectively probe the three distinctive types of oxygen atoms in V_2O_5.

Acknowledgments

SB acknowledges startup funding from the University at Buffalo for support of this work. JMV acknowledges support from the NSF-funded LSAMP Bridge to the Doctorate program. Certain commercial names are presented in this manuscript for purposes of illustration and do not constitute an endorsement by the National Institute of Standards and Technology.

References

(1) Law, M.; Goldberger, J.; Yang, P. *Annu. Rev. Mater. Res.* **2004**, *34*, 83.

(2) Nanowires and Nanobelts: Materials Properties and Devices Metal and Semiconductor Nanowires; Wang, Z. L., Ed.; Springer: New York, 2003; Vol. I.

(3) Lieber, C. M. *MRS Bull.* **2003**, *28*, 486.

(4) Samuelson, L. *Mater. Today* **2003**, *6*, 22.

(5) Dai, H. *Acc. Chem. Res.* **2002**, *35*, 1035.

(6) Cao, G. *Nanostructures & Nanomaterials: Synthesis, Properties & Applications*, 1 ed.; Imperial College Press: London, 2004.

(7) Ren, Z. F.; Huang, Z. P.; Xu, J. W.; Wang, J. H.; Bush, P.; Siegal, M. P.; Provencio, P. N. *Science* **1998**, *282*, 1105.

(8) Martin, C. R. *Science* **1994**, *266*, 1961.

(9) Velazquez, J. M.; Banerjee, S. *Small* **2008**, DOI: *10.1002/smll.200801278*.

(10) Mokerov, V. G.; Makarov, V. L.; Tulvinskii, V. B.; Begishev, A. R. *Opt. Spectrosc.* **1976**, *40*, 58.

(11) Allersma, T.; Hakim, R.; Kennedy, T. N.; Mackenzie, J. D. *J. Chem. Phys.* **1067**, *46*, 154.

(12) Winter, M.; Jurgen, O. B.; Spahr, M. E.; Novak, P. *Adv. Mater.* **1998**, *10*, 725.

(13) Murphy, D. W.; Christian, P. A.; DiSalvo, F. J.; Waszczak, J. V. *Inorg. Chem.* **1979**, *18*, 2800.

(14) Wang, Y.; Cao, G. *Chem. Mater.* **2006**, *18*, 2787.

(15) Livage, J. *Chem. Mater.* **1991**, *3*, 578.

(16) Eyert, V.; Hock, K.-H. *Phys. Rev. B* **1998**, *57*, 12727.

(17) Kolczewski, C.; Hermann, K. *Physica Scripta* **2005**, *T115*, 128.

(18) Chakrabarti, A.; Hermann, K.; Druzinic, R.; Witko, M.; Wagner, F.; Peterson, H. *Phys. Rev. B* **1999**, *59*, 10583.

(19) Whittingham, M. S. *J. Electrochem. Soc.* **1976**, *123*, 315.

(20) Sudant, G.; Baudrin, E.; Dunn, B.; Tarascon, J.-M. *J. Electrochem. Soc.* **2004**, *151*, A666.

(21) Baddour-Hadjean, R.; Raekelboom, E.; Pereira-Ramos, J. P. *Chem. Mater.* **2006**, *18*, 3548.

(22) Chan, C. K.; Peng, H.; Twesten, R. D.; Jarausch, K.; Zhang, X. F.; Cui, Y. *Nano Lett.* **2007**, *7*, 490.

(23) Li, W.; Garofalini, S. H. *J. Electrochem. Soc.* **2005**, *152*, A364.

(24) Rolison, D. R.; Dunn, B. *Chem. Mater.* **2001**, *11*, 963.

(25) Chain, E. E. *Appl. Opt.* **1991**, *30*, 2782.

(26) Forzatti, P. *Appl. Catal. A* **2001**, *222*, 221.

(27) Stohr, J. *NEXAFS Spectroscopy*; Springer: Berlin, 1992.

(28) Chen, J. G. *Surf. Sci. Reports* **1997**, *30*, 1.

(29) deGroot, F. M. F. G., M.; Fuggle, J. C.; Ghijsen, J.; Sawatzky, G. A.; Peterson, H. *Phys. Rev. B* **1989**, *40*, 5715.

(30) Banerjee, S.; Hemraj-Benny, T.; Sambasivan, S.; Fischer, D. A.; Misewich, J. A.; Wong, S. S. *J. Phys. Chem. B* **2005**, *109*, 8489.

(31) Hemraj-Benny, T.; Banerjee, S.; Sambasivan, S.; Balasubramanian, M.; Fischer, D. A.; Eres, G.; Puretzky, A. A.; Geoghan, D. B.; Lowndes, D. H.; Han, W. Q.; Misewich, J. A.; Wong, S. S. *Small* **2006**, *2*, 26.

(32) Blonska-Tabero, A. *J. Thermal Anal. Calorimetry* **2007**, *88*, 201.

(33) Kolasinksi, K. W. *Curr. Opin. Solid State Mater. Sci.* **2006**, *10*, 182.

(34) Abbate, M.; De Groot, F. M. F.; Fuggle, J. C.; Ma, Y. J.; T., C. C.; Sette, F.; Fujimori, A.; Ueda, Y.; Kosuge, K. *Phys. Rev. B* **1991**, *43*, 7263.

(35) Zaanen, J.; Sawatzky, G. A. *Phys. Rev. B* **1986**, *33*, 8074.

(36) Goering, E.; Muller, O.; Klemm, M.; denBoer, M. L.; Horn, S. *Philos. Mag. B* **1997**, *75*, 229.

(37) Park, T.-J.; Sambasivan, S.; Fischer, D. A.; Yoon, W.-S.; Misewich, J. A.; Wong, S. S. *J. Phys. Chem. C* **2008**, *112*, 10359.

(38) Kolczewski, C.; Hermann, K. *J. Chem. Phys.* **2003**, *118*, 7599.

(39) Kolczewski, C.; Hermann, K. *Surf. Sci.* **2004**, *552*, 98.

(40) Lambrecht, W.; Djafari-Rouhani, B.; Vennik, J. *J. Phys. C.* **1981**, *14*, 4785.

(41) Sakai, T.; Ishikawa, K.; Takezoe, H.; Matsuie, N.; Yamamoto, Y.; Ishii, H.; Ouchi, Y.; Oji, H.; Seki, K. *J. Phys. Chem. B* **2001**, *105*, 9191.

(42) Smith, A. P.; Ade, H. *Appl. Phys. Lett.* **1996**, *69*, 3833.

Figure Captions

Table 1. V *3d*—O 2*p* orbital overlaps calculated by Eyert and Hock based on an all-electron electronic structure calculation.[16]

Table 2. Orbital character of excited state levels and assignment of transitions to levels contributing to the three observed peaks in the O K-edge noted in Fig. 4 based on *ab initio* DFT calculations of a $V_{10}O_{31}H_{12}$ cluster model reported by Kolczewski and Hermann. The separate contributions from the three distinct types of oxygen atoms in V_2O_5 are shown separately.[38]

Figure 1. Schematic depiction of the crystal structure of orthorhombic V_2O_5. The yellow spheres represent V atoms, whereas the black spheres represent O atoms. (A) shows the layered structure of V_2O_5 based on zigzag double chains separated by a pronounced gap; (B) shows the unit cell of V_2O_5 depicting three kinds of oxygen atoms: terminal vanadyl oxygens (O1), bridging oxygen atoms (O2) involved in corner sharing, and chaining oxygen atoms (O3) involved in edge sharing. The unit cell dimensions are a = 11.519 Å, b = 4.373 Å, and c = 3.564 Å.

Figure 2. A,B) SEM images showing dense arrays of single-crystalline V_2O_5 nanowires grown on Si/SiO_2 substrates. C) High-resolution SEM image of the faceted tip of a nanowire. D) HRTEM image of the tip of a nanowire; the inset shows a lower resolution TEM image.

Figure 3. XRD patterns of micrometer-sized V_2O_5 powder compared to the pattern acquired for V_2O_5 nanowire arrays indicating the strong preferential growth direction of the nanowires.

Figure 4. V L-edge and O K-edge NEXAFS spectra of the single-crystalline V_2O_5 nanowires acquired at normal and grazing incidence. The peak assignments are based on data for single crystal V_2O_5 samples measured by Goering et al.[36]

Figure 5. Angle-dependent V L-edge data acquired for the V_2O_5 nanowire array.

Figure 6. A) Angle-dependent O K-edge data acquired for the V_2O_5 nanowire array. The t_{2g} peak clearly increases in intensity with increasing angle of incidence and the e_g peak shows an opposite trend. B) The O K-edge data acquired at grazing incidence is fitted using three Gaussian profiles for the three peaks Ox_1—Ox_3 noted in Fig. 4. See Table 2 for peak assignments to transitions to V 3*d*—O 2*p* states. C) Plot of the integrated area of the low-energy t_{2g} π peak versus the incident angle. The solid line depicts a cosine fit to the data points. D) Plot of the integrated area of the high-energy σ* peak versus the angle of incidence. The solid line depicts a cosine fit to the data points.

	Vanadyl V=O (O1) Terminal	*Bridging oxygen (O2) Corner sharing*	*Chaining oxygen (O3) Edge sharing*
V $3d_{xy}$	-	$2p_y$	$2p_x$, $2p_y$
V $3d_{xz}$	$2p_x$	$2p_z$	$2p_z$
V $3d_{yz}$	$2p_y$	$2p_z$	
V $3d_{x2-y2}$		$2p_x$, $2p_y$	$2p_x$
V $3d_{z2}$	$2p_z$		

Table 1. V *3d*—O 2*p* orbital overlaps calculated by Eyert and Hock based on an all-electron electronic structure calculation.[16]

	O(1) 1*s* excitation	**O(2) 1*s* excitation**	**O(3) 1*s* excitation**
Type of oxygen	*Vanadyl V=O*	*Bridging oxygen*	*Chaining oxygen*
Ox_1	O(1) p_y- V $3d_{yz}$ O(1) p_x- V $3d_{xz}$	O(2) p_y- V $3dx_y$	-
Ox_2+Ox_3	O(1) p_z- V $3d_{z2}$	O(2) p_x- V $3d_{x2-y2}$	O(3) p_x+p_y- V $3d_{x2-y2}$

Table 2. Orbital character of excited state levels and assignment of transitions to levels contributing to the three observed peaks in the O K-edge noted in Fig. 3 based on *ab initio* DFT calculations of a $V_{10}O_{31}H_{12}$ cluster model reported by Kolczewski and Hermann. The separate contributions from the three distinct types of oxygen atoms in V_2O_5 are depicted.[38]

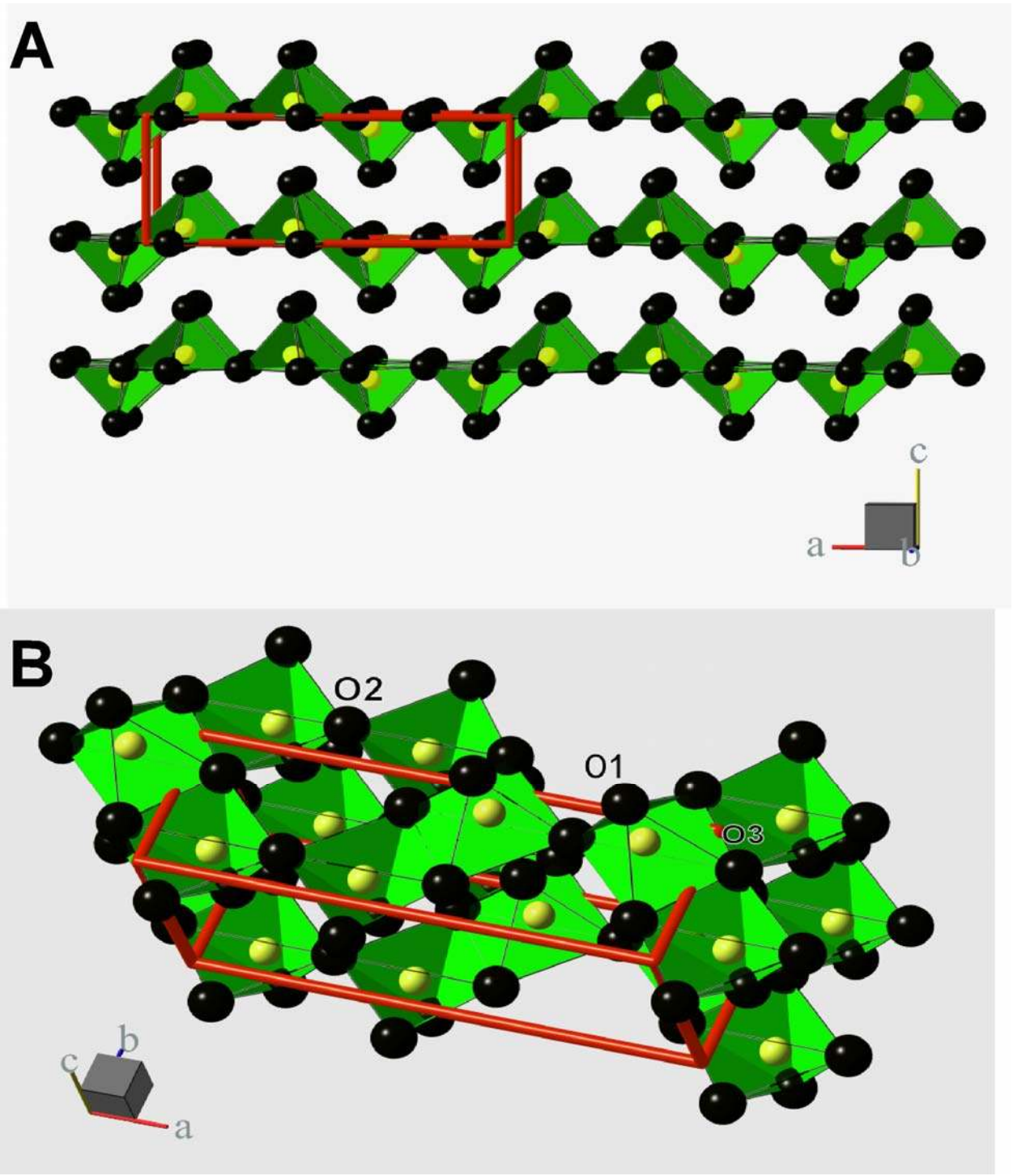

Figure 1. Schematic depiction of the crystal structure of orthorhombic V_2O_5. The yellow spheres represent V atoms, whereas the black spheres represent O atoms. (A) shows the layered structure of V_2O_5 based on zigzag double chains separated by a pronounced gap; (B) shows the unit cell of V_2O_5 depicting three kinds of oxygen atoms: terminal vanadyl oxygens (O1), bridging oxygen atoms (O2) involved in corner sharing, and chaining oxygen atoms (O3) involved in edge sharing. The unit cell dimensions are a = 11.519 Å, b = 4.373 Å, and c = 3.564 Å.

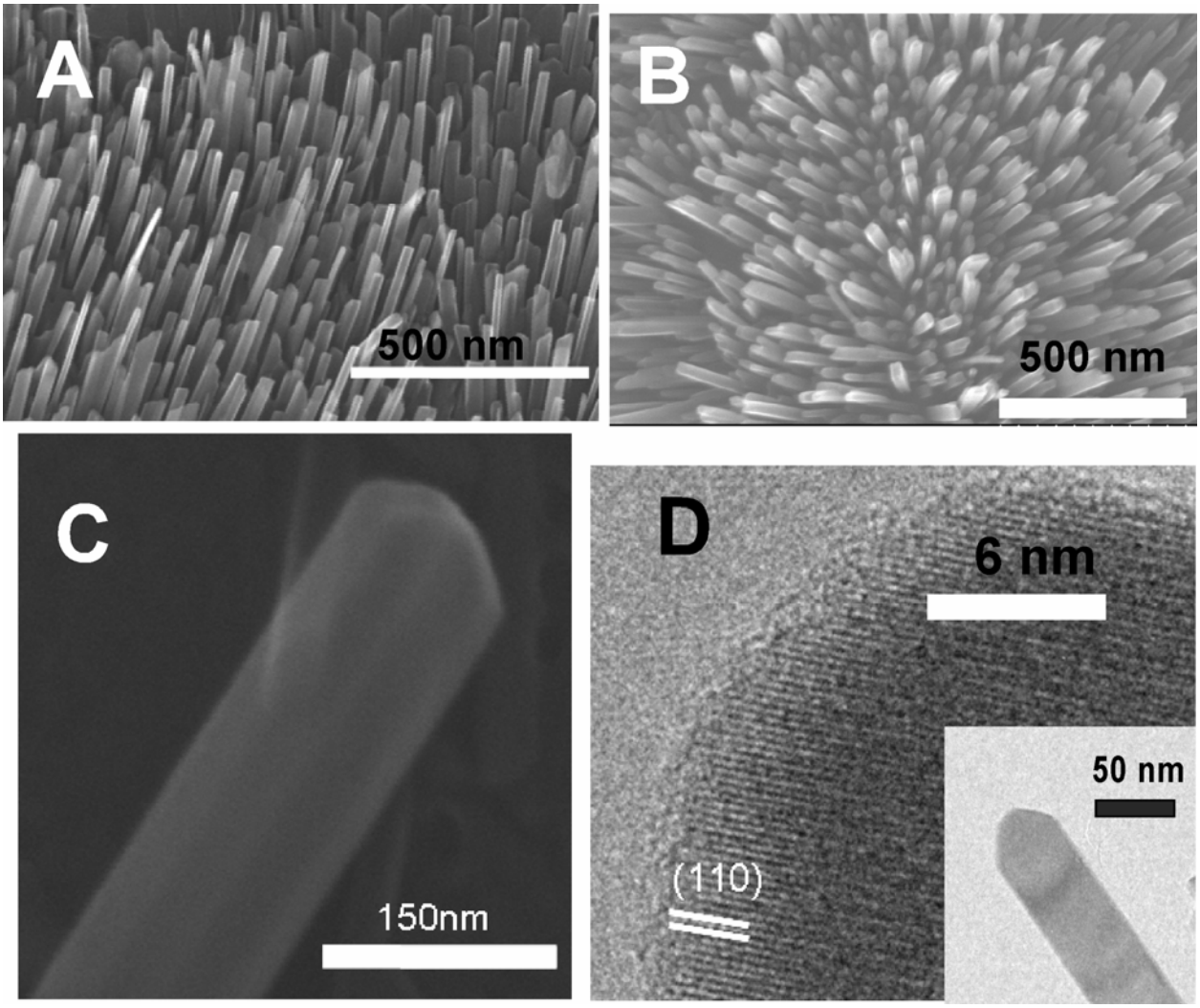

Figure 2. A,B) SEM images showing dense arrays of single-crystalline V_2O_5 nanowires grown on Si/SiO_2 substrates. C) High-resolution SEM image of the faceted tip of a nanowire. D) HRTEM image of the tip of a nanowire; the inset shows a lower resolution TEM image.

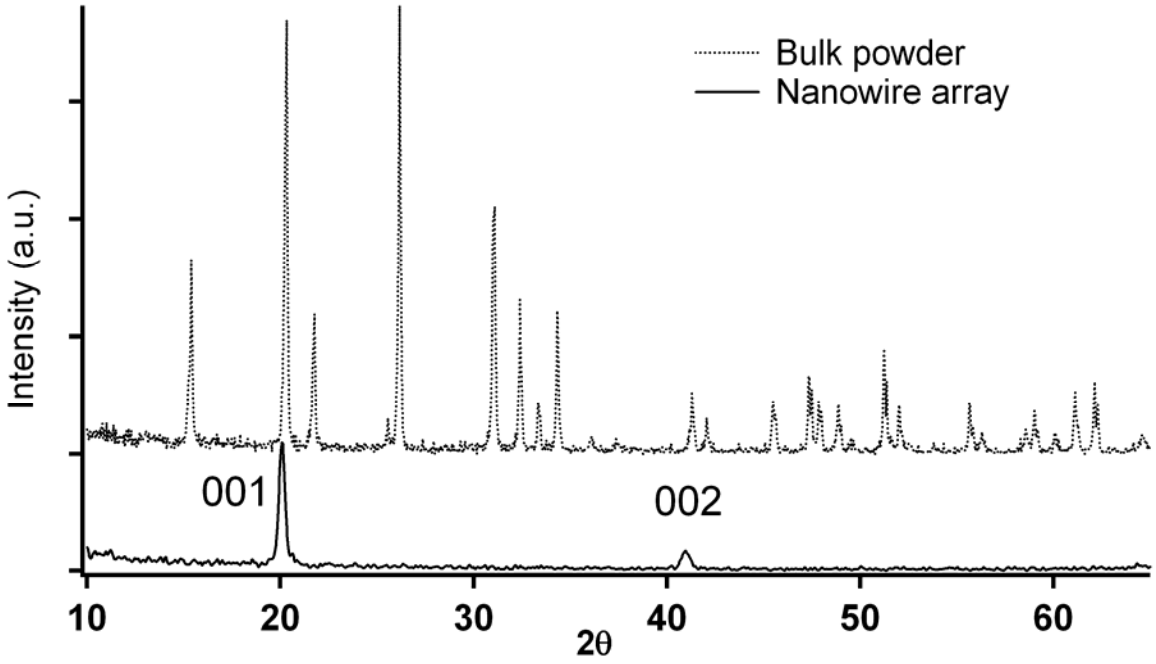

Figure 3. XRD patterns of micrometer-sized V_2O_5 powder compared to the pattern acquired for V_2O_5 nanowire arrays indicating the strong preferential growth direction of the nanowires.

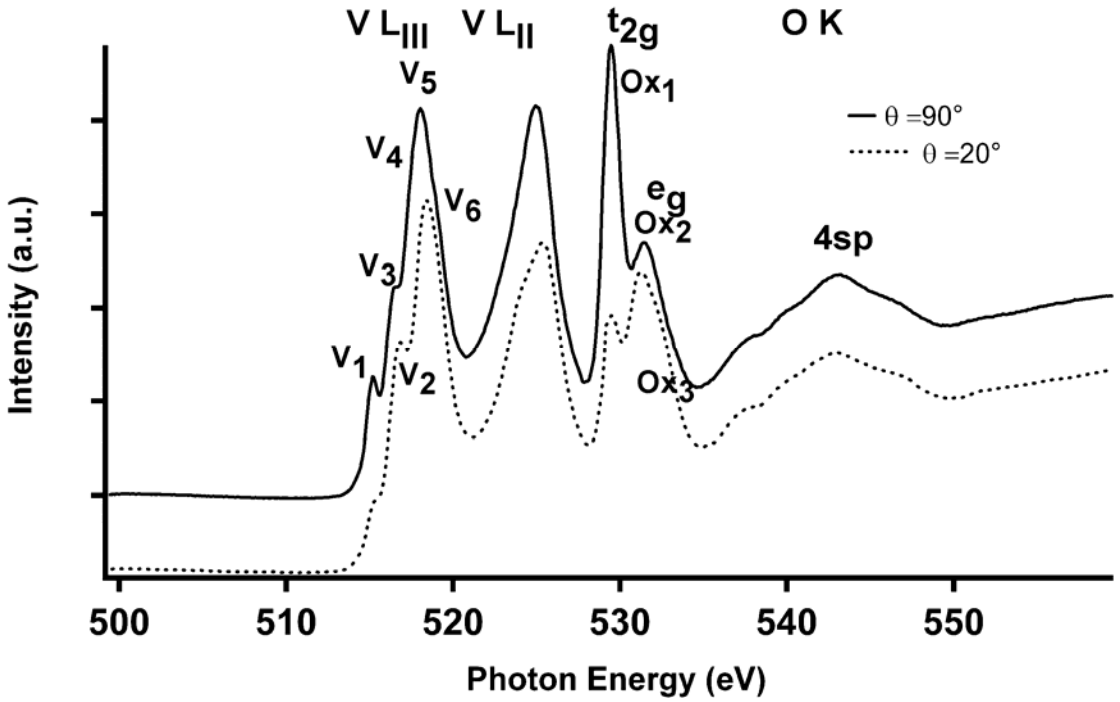

Figure 4. V L-edge and O K-edge NEXAFS spectra of the single-crystalline V_2O_5 nanowires acquired at normal and grazing incidence. The peak assignments are based on data for single crystal V_2O_5 samples measured by Goering et al.[36]

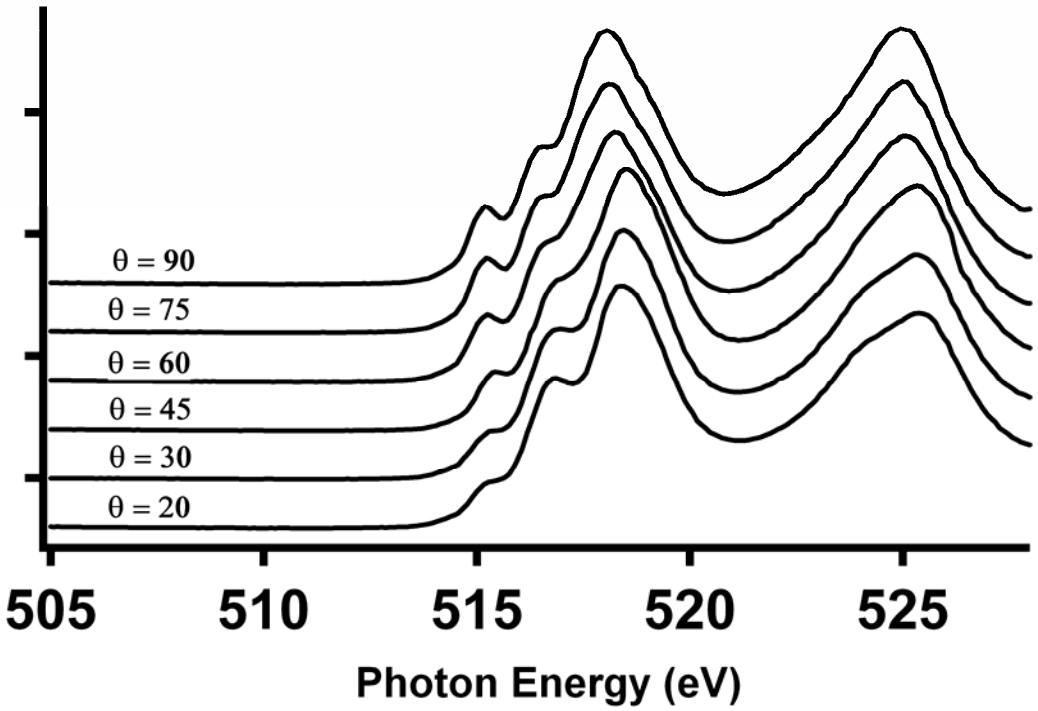

Figure 5. Angle-dependent V L-edge data acquired for the V_2O_5 nanowire array.

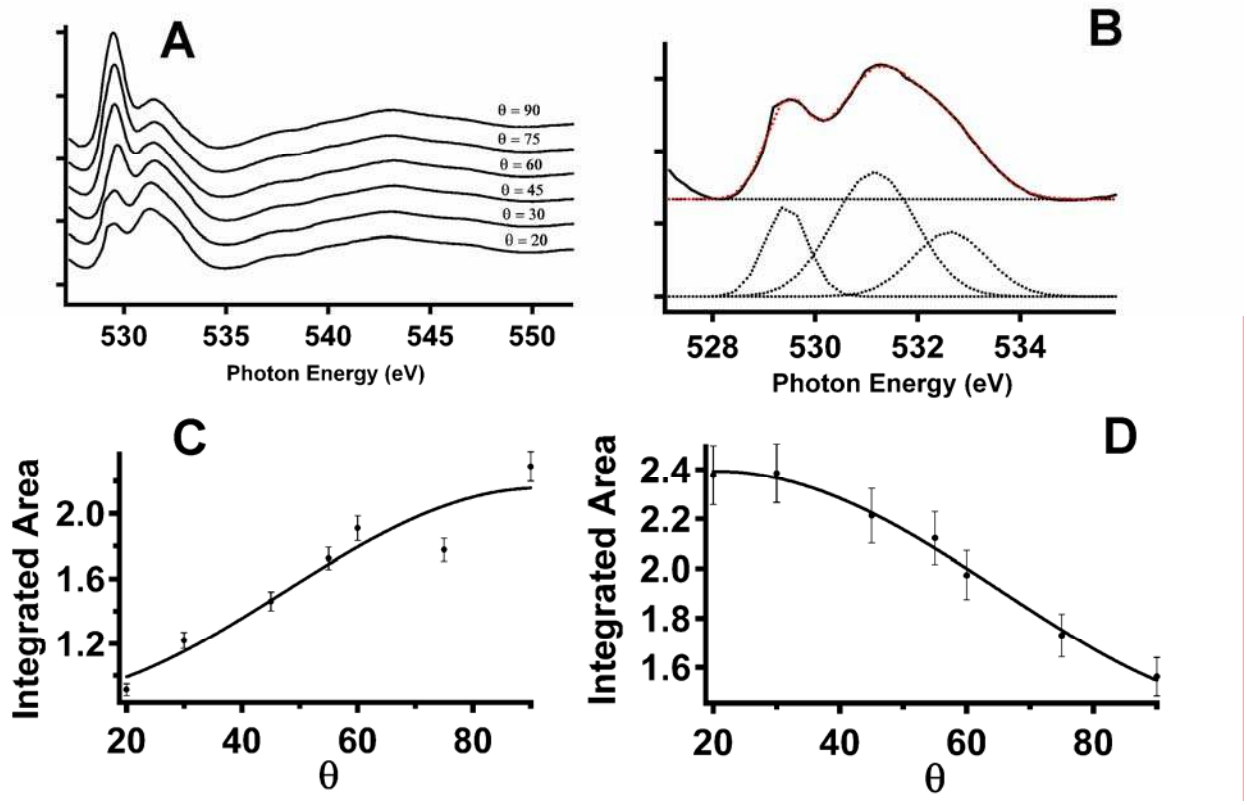

Figure 6. A) Angle-dependent O K-edge data acquired for the V_2O_5 nanowire array. The t_{2g} peak clearly increases in intensity with increasing angle of incidence and the e_g peak shows an opposite trend. B) The O K-edge data acquired at grazing incidence is fitted using three Gaussian profiles for the three peaks Ox_1—Ox_3 noted in Fig. 4. See Table 2 for peak assignments to transitions to V 3*d*—O 2*p* states. C) Plot of the integrated area of the low-energy t_{2g} π peak versus the incident angle. The solid line depicts a cosine fit to the data points. D) Plot of the integrated area of the high-energy σ* peak versus the angle of incidence. The solid line depicts a cosine fit to the data points.

Angle-dependent near-edge X-ray absorption spectroscopy is used to sensitively probe the electronic structure, alignment, and uniformity of crystal growth direction of V_2O_5 nanowire arrays fabricated by a novel metal-catalyzed vapor transport process. The obtained spectra verify theoretical predictions of the directionality and spatial orientation of the specific V 3*d* and O 2*p* orbitals contributing to the frontier orbital states of V_2O_5. Angle-dependent NEXAFS spectroscopy is also shown to be a useful probe for evaluation of the degree of alignment of the nanowire arrays.